Journal of Applied Physics

RESEARCH ARTICLE | AUGUST 25 2025

Electronic mobility, doping, and defects in epitaxial $BaZrS_3$ chalcogenide perovskite thin films

Jack Van Sambeek ; Jessica Dong ; Anton V. Ievlev ; Tao Cai ; Ida Sadeghi; R. Jaramillo

J. Appl. Phys. 138, 085703 (2025)
https://doi.org/10.1063/5.0284663
CHORUS

AIP Publishing

Journal of Applied Physics ARTICLE pubs.aip.org/aip/jap

Electronic mobility, doping, and defects in epitaxial $BaZrS_3$ chalcogenide perovskite thin films

Cite as: J. Appl. Phys. **138**, 085703 (2025); doi: 10.1063/5.0284663
Submitted: 9 June 2025 · Accepted: 4 August 2025 ·
Published Online: 25 August 2025

Jack Van Sambeek,[1] Jessica Dong,[1] Anton V. Ievlev,[2] Tao Cai,[1] Ida Sadeghi,[1] and R. Jaramillo[1,a)]

AFFILIATIONS

[1]Department of Materials Science and Engineering, Massachusetts Institute of Technology, Cambridge, Massachusetts 02139, USA
[2]Center for Nanophase Material Sciences, Oak Ridge National Laboratory, Oak Ridge, Tennessee 37830, USA

[a)]**Author to whom correspondence should be addressed:** rjaramil@mit.edu

ABSTRACT

We present the electronic transport properties of $BaZrS_3$ thin films grown epitaxially by gas-source molecular beam epitaxy. We observe *n*-type behavior in all samples, with carrier concentration ranging from 4×10^{18} to 4×10^{20} cm^{-3} at room temperature (RT). We observe a champion RT Hall mobility of 11.1 $cm^2\,V^{-1}\,s^{-1}$, which is competitive with established thin-film photovoltaic absorbers. Temperature-dependent Hall mobility data show that phonon scattering dominates at room temperature, in agreement with computational predictions. X-ray diffraction data illustrate a correlation between mobility and antiphase boundary concentration, illustrating how microstructure can affect transport. Despite the well-established environmental stability of chalcogenide perovskites, we observe significant changes to electronic properties as a function of storage time in ambient conditions. With the help of secondary ion mass spectrometry measurements, we propose and support a defect mechanism that explains this behavior: as-grown films have a high concentration of sulfur vacancies that are shallow donors ($V_S^{\cdot}$ or $V_S^{\cdot\cdot}$), which are converted into neutral oxygen defects ($O_S^{\times}$) upon air exposure. We discuss the relevance of this defect mechanism within the larger context of chalcogenide perovskite research, and we identify means to stabilize the electronic properties.

INTRODUCTION

Chalcogenide perovskite semiconductors are of interest as absorbers for thin-film photovoltaics (PV). Chalcogenide perovskites are distinguished by their Earth-abundant elements, low-to-no toxicity, thermo-chemical stability, strong optical absorption, and direct bandgap (E_g) that can be tuned continuously by alloying.[1–7] $BaZrS_3$ (BZS, with $E_g = 1.9$ eV) is by far the most-studied chalcogenide perovskite, with decades of publications reporting synthesis of samples with different form factors (powder, single crystals, nanoparticles, polycrystalline thin films, and epitaxial thin films) and properties including photoluminescence and dielectric susceptibility.[1,3,5,7–20] However, the electronic properties of BZS remain little-reported. Measuring and understanding the electronic properties of BZS, and by extension of chalcogenide perovskites more broadly, is an important next step in the development of these materials for PV.

Published reports on the electronic properties of chalcogenide perovskites suggest that they are likely but not necessarily *n*-type. A recent computational study by Yuan *et al.* predicts that the dominant intrinsic dopants in BZS are S vacancies, which are shallow double donors and are responsible for *n*-type conductivity. Yuan *et al.* also predict that the electron mobility (μ) at room temperature (RT) is phonon-limited to 37 $cm^2\,V^{-1}\,s^{-1}$.[21] These theoretical predictions are consistent with experimental observations: at least two publications report large electron concentration ($n > 10^{20}$ cm^{-3}) in BZS thin films, and Aggarwal *et al.* provide evidence that *n* is positively correlated with S deficiency.[12,22] Hanzawa *et al.* reported synthesis of both *n*- and *p*-type $SrHfS_3$ by aliovalent doping.[23] This is encouraging for achieving ambipolar doping in chalcogenide perovskites more broadly, especially because $SrHfS_3$ has a rather wide bandgap (2.3 eV), that ought to make it more difficult to achieve ambipolar doping than for compounds with smaller bandgap. Less is known about the mobility and how it

might be improved in thin films. *n*-type mobility exceeding 10 $cm^2 V^{-1} s^{-1}$ has been reported.[12] Experimental studies of the mobility-limiting mechanisms have not been reported.

RESULTS

In this work, we leverage a large set of epitaxial BZS thin films, and complementary experiments including Hall effect measurements, x-ray diffraction, and secondary ion mass spectroscopy (SIMS), to gain a more complete understanding of electronic transport. The sample set spans an area of processing parameter space, owing to both intentional variation of processing conditions, and undesirable growth-to-growth variations induced by equipment limitations. The resulting films are, thus, meant to provide an understanding of the range of growth outcomes and electronic transport properties obtainable in BZS. As grown, our BZS films have widely varying electronic properties, with four-point probe measured sheet resistance (R_S) values ranging from below 1 kΩ/□ to more than 1 GΩ/□. In Fig. 1, we present Hall measurement results for a large number of samples that are sufficiently

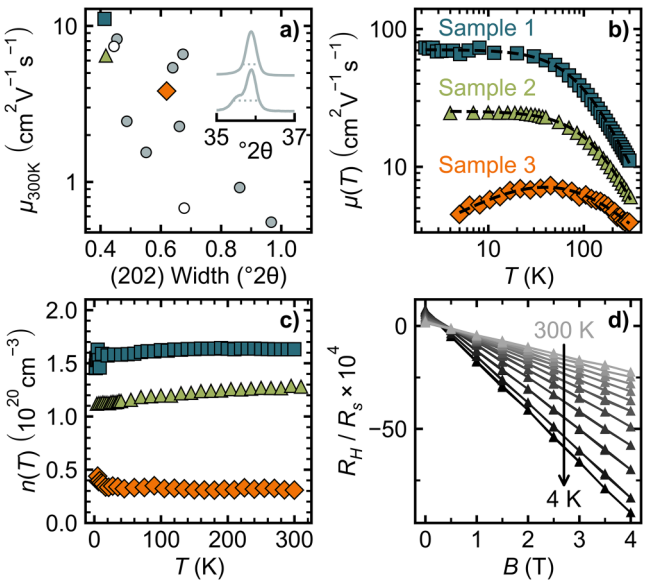

FIG. 1. Hall effect measurement results for a distribution of $BaZrS_3$ thin films. (a) Hall mobility at 300 K plotted against HRXRD-measured (202) full-width at one quarter max (FWQM). The inset shows the (202) peak shape for the two samples indicated by hollow markers, with horizontal dashed lines showing their FWQM. (b) Temperature-dependent Hall mobility for samples 1–3. Dashed curves show fits to the expression: $\mu^{-1} = AT^{\alpha} + BT^{\beta}$, which is a Matthiessen's rule addition of two power-law mobility trends. For samples 1 and 2, α is −1.6 and β is 0. For sample 3, α and β are −0.7 and 0.4, respectively. (c) Temperature-dependent electron concentration for samples 1–3. (d) Field-dependence of Hall measurements for sample 2 shown at temperatures in the range 4–300 K. The ordinate is Hall resistance (R_H) divided by sheet resistance (R_S), scaled by a factor of 10^4. In all panels, squares correspond to sample 1, triangles to sample 2, and rotated squares to sample 3. Circles indicate other samples for which further characterization is not included in this report.

conductive ($R_S < \sim 1$ MΩ/□) for our instrumentation. These data were recorded shortly after synthesis of each sample. We observe exclusively *n*-type behavior, with large RT carrier concentration *n* (300 K) in the range $4 \times 10^{18} - 4 \times 10^{20}$ cm^{-3} (Fig. S1 in the supplementary material). We observe a champion RT Hall mobility μ(300 K) of 11.1 $cm^2 V^{-1} s^{-1}$, which is on par with established thin-film PV absorbers including lead-halide perovskites.[24] This champion film (sample 1) also shows strong room-temperature PL in comparison to other samples (even those with significantly larger carrier densities), suggesting a relatively slow rate of non-radiative recombination (Fig. S2 in the supplementary material).

We observe a wide distribution in μ across all films measured, extending to below 0.5 $cm^2 V^{-1} s^{-1}$. In general, we expect that μ will be lower for films with broader x-ray diffraction peak widths, as peak width grows with increasing concentrations of extended defects. Several of the lesser-quality films show a low-angle shoulder on the (202) XRD peak [Fig. 1(a), inset]. Our previous reports attributed this (202) peak shoulder to the presence of antiphase boundary (APB) defects, which are expected to impede carrier transport. To illustrate the correlation of transport with film defect concentration, in Fig. 1(a), we plot μ at 300 K against the full-width at one quarter max (FWQM) of the (202) peak. FWQM is sensitive to symmetric peak broadening and to the low-angle shoulder, unlike the more commonly used full-width at half-maximum (FWHM) that does not well capture low-intensity shoulders. The data in Fig. 1(a) show that μ is strongly reduced with increasing FWQM. Figure 1(a) highlights the need for continuous improvement in film growth process control.

We performed temperature-dependent Hall measurements on a subset of the films shown in Fig. 1(a) to investigate the dominant mobility-limiting mechanisms. In Fig. 1(b), we present temperature-dependent Hall mobility data [$\mu(T)$] for three samples, referred henceforth as samples 1–3. We find that the electron concentration for each sample [$n(T)$] is approximately temperature-independent across the entire measured range from 4 to 300 K [Fig. 1(c)]. Such weak temperature dependence of $n(T)$ is expected in the degenerate doping limit and has been reported previously in this material system.[22]

Near room temperature, all three samples show decreasing μ with increasing temperature, which identifies phonon scattering as the mobility-limiting mechanism, consistent with recent computational predictions.[21,25] Samples 1 and 2, with larger carrier concentration and lower (202) peak FWQM, display prototypical features of metallic conduction: phonon-limited mobility near room temperature, transitioning to temperature-independent, defect-limited mobility at cryogenic temperature. Sample 3, with smaller carrier concentration and larger (202) peak FWQM, shows $\mu(T)$ behavior intermediate between the metallic and non-degenerate doping limits, possibly due to its lower carrier density. Upon cooling, $\mu(T)$ reaches a maximum value of 7 $cm^2 V^{-1} s^{-1}$ around 50 K. Further cooling causes μ to decrease, though at a slower rate than the $T^{3/2}$ behavior expected from ionized-impurity scattering in non-degenerate semiconductors.[25] In contrast to these three epitaxial samples, we observe non-metallic behavior in both *n* and μ for a polycrystalline film sample (sample P1) grown on Al_2O_3, despite its nearly ten times larger room-temperature *n* of 3×10^{21} cm^{-3} (Fig S3 in the supplementary material). Sample P1 shows strongly

temperature-dependent n over a two-decade range, and $\mu(T)$ varies between 0.1 and 0.9 $cm^2 V^{-1} s^{-1}$ with low-temperature behavior indicative of ionized-impurity scattering. This unexpected result suggests that perhaps high-angle and random grain boundaries change the conditions for metallicity in $BaZrS_3$.

Despite the established air stability of $BaZrS_3$, and of chalcogenide perovskites broadly, we observe significant instabilities in electrical properties during storage under ambient conditions. R_S for each sample increases monotonically over time, with a rate that varies strongly sample-to-sample. For some samples, R_S increases as quickly as one decade per week, and for others as slowly as doubling over several months [Fig. 2(a)]. This behavior occurs without any associated structural changes. In Fig. 2, we demonstrate the effects of storage in ambient conditions on sample 1, as a representative case. For this sample, the four-point-probe measured R_S increased from 720 Ω/□ as-grown to 1.6 kΩ/□ after 75 days of storage. We recorded high-resolution x-ray diffraction (HRXRD) measurements of the film (202) peak within one day of growth and repeated 285 days later. We observed no significant change in peak shape or position [Fig. 2(c)], demonstrating little-to-no structure change due to long-term storage in air. To understand the observed changes in electronic transport, we performed temperature-dependent Hall measurements on this sample, once three days after synthesis (data in Fig. 1), and again 72 days later. We compare the $n(T)$ curves in Fig. 2(b). In both measurements, we observe n-type behavior with n nearly independent of temperature. We observe a 25% reduction in n after sample storage from 1.6×10^{20} to 1.2×10^{20} cm^{-3}. $\mu(T)$ data [Fig. 2(d)] shows that μ is lower after storage but also that the temperature-dependence $\mu(T)$ is unchanged, suggesting that the dominant mobility-limiting mechanisms remained the same.

To explain these effects of sample storage in air, we hypothesize a simple defect mechanism,

$$V_S^{\cdot\cdot} + 2e^- + \frac{1}{2}O_{2(g)} \rightarrow O_S^{\times}, \quad (1)$$

in which ambient oxygen fills vacant anion sites, converting V_S donors to O_S defects, which are predicted to be electrically neutral.[21] Because the films are very thin (<50 nm), and the sulfur vacancy concentration is quite large (approaching 1% of sulfur sites), it is reasonable to expect rapid anion diffusion, which explains how oxygen exposure at room temperature can affect film properties on the time scale of weeks.

We conducted annealing experiments to further understand the aging mechanisms and to explore post-growth defect control. Samples A1–A4 were annealed in a vacuum tube furnace under a range of H_2S gas flow (0–10 SCCM) and a range of temperature (150–500 °C). Sample A5 was annealed in an ultrahigh vacuum chamber at 200 °C while exposed to an H_2S plasma. We report detailed annealing conditions in Table S1 in the supplementary material. All annealed samples showed at least one order-of-magnitude increase in R_S following annealing, with samples A3 and A4 becoming immeasurably resistive [Fig. 3(a)]. Only samples A2 and A5 remained conductive enough to enable post-anneal Hall measurements. These samples showed reductions in both n (1.2×10^{20} to 1.9×10^{19} cm^{-3} for sample A2 and 6.9×10^{20} to 6.7×10^{19} cm^{-3} for sample A5) and μ (8.2 to 1.1 $cm^2 V^{-1} s^{-1}$ for sample A2 and 2.3 to 0.32 $cm^2 V^{-1} s^{-1}$ for sample A5). The reduction in μ is notable as this would be unexpected if the annealing process was incorporating sulfur into the film to heal V_S defects. Instead, it seems likely that the annealing treatments are simply accelerating the aging effects observed during

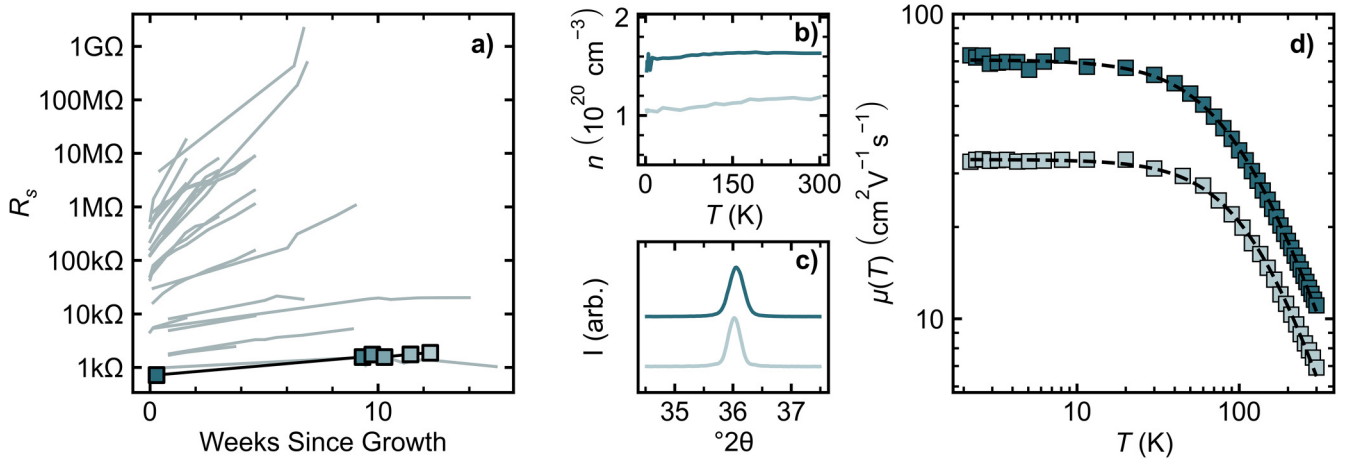

FIG. 2. Time-evolution of properties after storage in ambient conditions. (a) Repeated four-point probe R_S measurements for sample 1 (blue squares) and a large set of BZS films (light gray lines) as a function of time from sample fabrication. (b) Temperature-dependent electron concentration, as-grown and after 75 days of storage for sample 1. (c) HRXRD measurements as-grown and after 285 days of storage for sample 1. (d) Temperature-dependent Hall mobility, as-grown and after 75 days of storage for sample 1. Dashed curves show fits to the same dual-power-law expression used in Fig. 1(b); here, α is −1.6 as-grown and −1.8 after storage, with β being 0 in both cases. In panels (b)–(d), the upper, darker data are the as-grown measurement; the lighter, lower data are the measurement after storage.

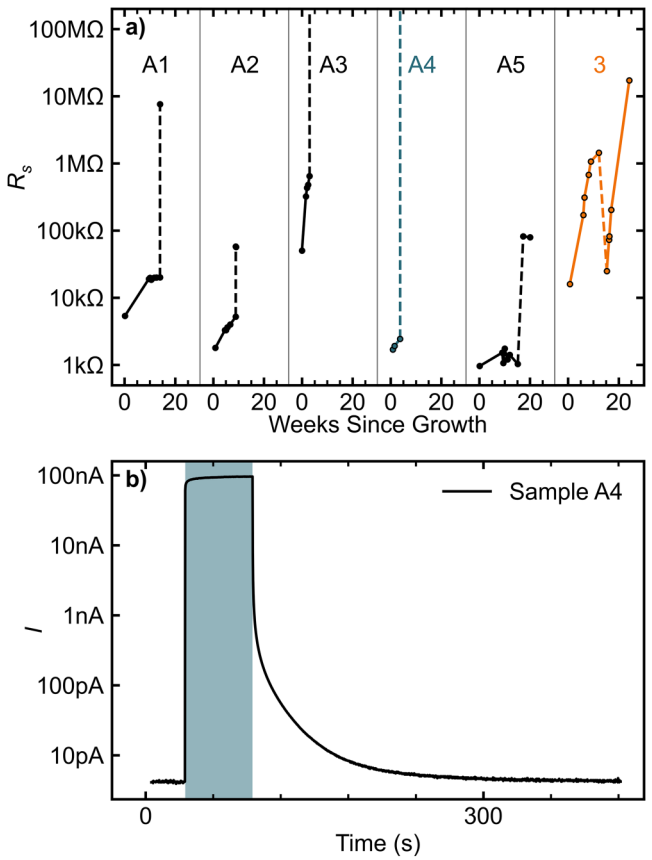

FIG. 3. Effects of annealing on electronic properties. (a) Repeated four-point probe R_s measurements as a function of time from fabrication for samples A1–A5 and sample 3. Solid connecting lines show changes during storage in ambient conditions, while broken lines show changes brought on by annealing treatments. Samples A3 and A4 were immeasurably resistive after annealing. (b) Post-anneal photocurrent measurement of sample A4 under 1 V of applied bias. The sample was illuminated by a white LED light source with an irradiance of 100 mW cm^{-2} during the period indicated by the shaded rectangle.

ambient storage by converting V_S to O_S. This may be possible even in oxygen-free annealing environments if the film native oxide layer (see below) acts as an oxygen source during annealing.

In addition to samples A1–A5, sample 3 was annealed at 400 °C in a load-locked semiconductor processing furnace under a high flow rate of PH_3 gas. This processing scheme should limit oxygen reactivity in comparison to the other processing methods, owing to the superior furnace quality and more reducing atmosphere. Indeed, we observe that unlike the other annealed samples, the resistance of sample 3 was significantly lowered by annealing [Fig. 3(a)], akin to the annealing outcomes recently reported by Aggarwal *et al.*[22] We suspect that this annealing treatment had minimal V_S to O_S conversion, and instead increased the V_S concentration either by liberating oxygen from existing O_S defects or by removing sulfur from the film. After annealing, R_S once again began rapidly increasing over time while the sample was stored in ambient conditions, consistent with our proposed V_S to O_S defect mechanism.

Post-anneal Hall measurements were not possible on samples A1, A3, and A4, so changes to n and μ for these samples cannot be directly quantified. In Fig. 3(b), we show the post-anneal photoconductivity response for sample A4, which had $R_S = 1.7$ kΩ/□ as-grown, and became immeasurably resistive after annealing. The four-decade-large photocurrent response measured post-anneal shows that the sample still has finite mobility and useful semiconductivity, confirming that the immeasurably large R_S is due to a reduction in the μn product, rather than morphological changes disrupting the film's connectivity. This finding agrees with scanning electron microscopy (SEM) micrographs of as-grown and post-anneal films, showing no appreciable microstructural changes (Fig. S6 in the supplementary material). However, without specific knowledge of changes in n and μ, the photoconductivity measurements alone are inconclusive as to whether the high-resistance samples underwent the same oxygen incorporation mechanism as suspected for samples A2 and A5. We must turn to compositional measurements to further understand the defect mechanisms at play.

To augment the electronic measurements of annealed samples, we performed time-of-flight secondary ion mass spectrometry (ToF-SIMS) depth profiling of samples A1–A5, and an additional sample that was not annealed (sample N). Due to a lack of suitable reference films of standard composition, the ToF-SIMS results are semiquantitative. While measured secondary ion intensities are linear to actual element concentrations, it impossible to calculate actual concentrations from ToF-SIMS data only, without calibration. Therefore, we cannot quantify atomic concentrations but can analyze relative composition comparisons between samples. We calibrated ion etch rates using atomic-force microscopy on sample N (Fig. S5 in the supplementary material) and used the measured etch rate to determine the measurement depth for each cycle in the ToF-SIMS measurements. Film thicknesses were determined from the depth-calibrated SIMS data and are shown in Table S1 in the supplementary material. We present in Fig. 4(a) depth-resolved elemental signal intensity line scans for sample A1 (see Fig. S4 in the supplementary material for line scans of all other samples). An oxygen-rich layer is apparent near the film surface, with rapidly decreasing oxygen signal as depth increases. This layer is consistent with our prior report of a self-limiting native oxide.[13] Beyond this surface layer, the signals of Ba, Zr, and S are well defined and constant until reaching the substrate. Oxygen is clearly present in the bulk of the film with the non-uniform signal intensity. Analysis of samples A2, A4, and A5 is complicated by the incomplete film coverage of these samples (Fig. S7 in the supplementary material). For these partially open films, O signal observed within the depth of the film could either be from impurities in the film or from exposed regions of the oxide substrate. We discuss this complication in Note 1 in the supplementary material; we conclude that excluding the bottom 5 nm of each film allows us to confidently attribute the measured O signal to the film rather than the substrate.

We use the ToF-SIMS data to test the hypothesis that annealing-induced electronic changes are due to O incorporation.

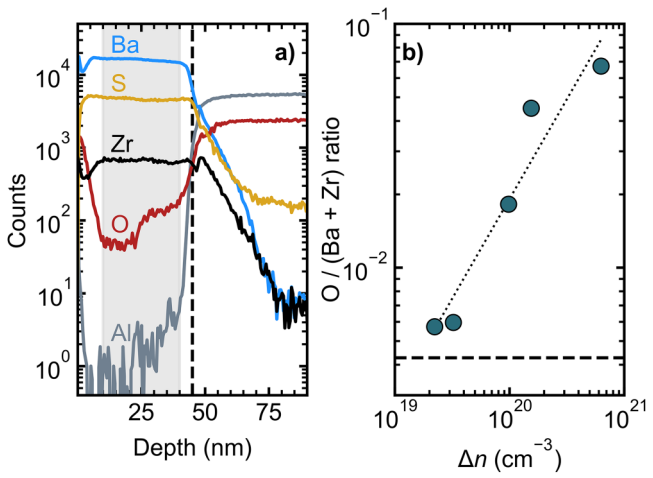

FIG. 4. Identifying the effect of oxygen uptake on carrier concentration. (a) ToF-SIMS depth profiles for sample A1 showing count rates for Ba, S, Zr, O, and Al secondary ions as a function of etching depth. The vertical dashed line indicates the film–substrate interface. The shaded gray area marks the depth range used for averaging. (b) Trend of oxygen content vs reduction in carrier concentration due to annealing. The ordinate shows the ratio of O signal to combined Ba and Zr signal measured by ToF-SIMS. The dashed horizontal line shows the same average for an unannealed film measured 85 days after it was grown. The abscissa shows the reduction in electron concentration observed between pre- and post-anneal measurements. The dashed line is a power-law fit with an exponent of 0.8 (0.1 standard error).

If annealing converts V_S to O_S defects, then the observed decrease in n should correlate with the post-anneal O concentration. The log–log plot presented in Fig. 4(b) shows the expected trend, with a power-law fit yielding a near-linear exponent of 0.8 ± 0.1. The ordinate is the average ratio between oxygen and combined Ba and Zr signals in the bulk of each film, which we use as a proxy for the ratio between oxygen concentration and anion site density. The abscissa is the n reduction as a result of annealing, according to Hall measurements. For films that were too resistive for post-anneal Hall measurements, we assume that post-anneal n was much smaller than the initial n. We list in Table S1 in the supplementary material the values of pre- and post-anneal n for each sample. The clear correlation shown in Fig. 4(b) is consistent with the proposed defect mechanism.

DISCUSSION AND CONCLUSION

Our results, particularly those shown in Fig. 1(a), emphasize the importance of continued improvements to film growth process control. The data show wide sample-to-sample variability. The highest-quality films are promising, and we do not know how much better the films could be with improved synthesis methods. At present, equipment limitations inhibit robust stoichiometry control and prevent reliable synthesis of the highest-quality films. Slight unintentional variations in growth conditions (e.g., flux ratios) can result in large changes to film properties due to altered point defect and extended defect populations. In particular, our results identify sulfur vacancies and APBs as important defects for our synthesis regime. This highlights that while we and others have achieved reliable phase control in chalcogenide perovskite synthesis, achieving precise control over stoichiometry and defects remains an outstanding challenge. Promising directions include reducing growth temperature and employing alternative precursors. For example, film synthesis using an organosulfur precursor was recently reported by Surendran *et al.* to improve chalcogenide film growth outcomes.[26] Similarly, we are currently developing synthesis by metal-organic molecular beam epitaxy (MOMBE) using an organozirconium precursor. Through this approach, we anticipate greater stoichiometry control, enhanced reaction kinetics, and reduced growth temperature.

There are several promising approaches to controlling sulfur defect concentrations in particular, including post-growth annealing. We recently found that annealing in H_2S plasma immediately following film growth, before air exposure, may yield films with orders-of-magnitude smaller carrier concentration and superior air stability (unpublished results). Reducing film growth temperature is also likely to lower the vacancy concentration. There is also likely need to improve control over cation defects in this ternary system, although the impacts of Ba- and Zr-based defects on film properties remain uncertain. We expect that continued innovations in chemical synthesis pathways, coupled with more robust processing controls, will produce substantial gains in defect control and film properties.

It remains unknown how high the electronic transport mobility of $BaZrS_3$ can be, and what range of carrier type and concentration can be achieved in thin films. We find here that room-temperature mobility is phonon-limited, even for highly doped films. This is consistent with two of our prior observations, of very high dielectric constant, and rather low optical phonon frequency.[20,27] We are not aware of a framework to calculate the mobility of highly polarizable semiconductors in the degenerate doping limit, this may be an opportunity for theory development. Of course, for device development, it will be important to reduce the carrier concentration and ideally to make both n- and p-type films. The successful demonstration of ambipolar doping in $SrHfS_3$ powder samples is encouraging for achieving similar in $BaZrS_3$ thin films.[23] Our results here suggest that sulfur vacancy concentration must be first minimized before aliovalent doping strategies are likely to succeed.

METHODS

We grow films on $LaAlO_3$ substrates by gas-source MBE at nominal substrate temperature of 900–1000 °C following our previously reported growth procedures (see Table S2 in the supplementary material for growth conditions).[13] Resulting film thicknesses are typically between 20 and 40 nm depending on specific growth parameters. HRXRD was measured using a Bruker D8 diffractometer configured with a Cu x-ray source and scintillation point-detector.

Sheet resistance measurements were done by linear four-point probe using a Signatone Pro4 test stand and Keithley 2601B source-measure unit. Samples with measurable conductivity undergo van der Pauw Hall measurements using a Lakeshore

Cryotronics M91 FastHall measurement controller with a Quantum Design Physical Properties Measurement System (PPMS) for temperature and magnetic field control. Bidirectional sweeps of the magnetic field were performed for each measurement, with magnitudes of at least 2 T. Larger field values were used as-needed to ensure adequate signal-to-noise ratios. Ti (5 nm)/Au (200 nm) electrical contact pads were deposited on samples by sputtering and then contacted using a Van der Pauw press-contact assembly with spring-loaded gold pins (Wimbush Science and Technology). For sufficiently conductive samples, direct contact with the press-contact assembly provided suitable ohmic contacting behavior, so sputtered contacts were not needed.

Tube furnace annealing was performed in a vacuum-assisted quartz tube furnace with a 40 mm outer diameter tube. After loading each sample, three pump/purge cycles were performed with Ar purge gas (typical base pressures were 3–20 mTorr). H_2S flow was initiated at the selected flow rate before ramping to process temperature at approximately 10 °C/min. After holding for 30 min at the process temperature, the furnace was allowed to cool naturally with the process gas flow maintained.

Ultrahigh vacuum (UHV) H_2S plasma annealing was performed in our MBE growth chamber (10^{-8} Torr base pressure). After about 15 weeks of air exposure, sample A5 was reloaded into the UHV chamber. With the substrate unheated, an H_2S plasma was ignited in a SPECS RF source and ramped to a forward power of 600 W. While under plasma exposure, the substrate was heated to 200 °C, held for 30 min, and then cooled naturally. Plasma source ramp-down began once the substrate temperature dropped below 65 °C.

Photoconductivity was measured using a Keithley 6517b electrometer under 1 V of applied bias. Illumination was provided by a Thorlabs SOLIS-1 A 6500K cold white LED driven at 5 A, resulting in an irradiance of 100 mW/cm^2 at the sample plane as measured by a Thorlabs S310C thermal power sensor.

SEM image acquisition was done in a Zeiss Gemini 450 field-emission SEM operating at 1.5 kV accelerating voltage using the Everhart Thornley secondary-electron detector.

ToF-SIMS measurements were carried out using TOF SIMS[5]-NSC instrument (IONTOF GmbH), which combines mass spectrometer with atomic-force microscope in the same vacuum chamber with vacuum levels $1–5 \times 10^{-8}$ mbar. Bi_3^+ liquid metal ion gun (30 keV energy, ~0.5 nA current in DC mode, 120 nm spot size) was used as a primary ion source to extract secondary ions from the surface of studied sample. This was complemented by Cs^+ sputter ion source (1 keV energy, 80 nA current, and 10–20 mm spot size). Measurements were carried out in non-interlaced mode, where each scan by Bi_3^+ (100×100 mm^2, 2.4 s) was followed by sputtering cycle with Cs^+ (500×500 mm^2, 3.3 s). Atomic-force microscopy was further used to measure depth of the resulting craters and further calibrate depth profiles measured by ToF-SIMS.

Steady-state photoluminescence spectroscopy (PL) was performed using a Horiba SMS spectroscopy system fitted with a 10× infinity-corrected objective, iHR320 spectrometer, 600 gr/mm 750 nm blaze holographic grating, and Syncerity silicon CCD. BZS samples were excited with both 405 and 635 nm Horiba DeltaDiode lasers to probe surface and bulk behavior, respectively. Measurements remove laser signal using appropriate longpass filters.

SUPPLEMENTARY MATERIAL

See the supplementary material for additional details including 300 K carrier concentration trends, photoluminescence data for sample 1, temperature-dependent Hall data for sample P1, a table of full annealing conditions, SEM images depicting sample morphology, and the full data set of SIMS depth profiles.

ACKNOWLEDGMENTS

This research was supported by the Air Force Office of Scientific Research under Grant No. FA9550-23-1-0695. This research was supported in part by the United States–Israel Binational Science Foundation (BSF) under Grant No. 2020270. This research was supported in part by the National Science Foundation (NSF) under Grant No. DMR-2224948. This research was supported in part by the Sagol Weizmann-MIT Bridge Program. J.V.S. and J.D. acknowledge support from the National Science Foundation Graduate Research Fellowship, Grant No. 1745302. We acknowledge support from AFOSR under Award No. FA9550-23-1-0157. ToF-SIMS characterization was conducted at the Center for Nanophase Materials Sciences, which is a DOE Office of Science User Facility, and using instrumentation within ORNL's Materials Characterization Core provided by UT-Battelle, LLC under Contract No. DE-AC05-00OR22725 with the U.S. Department of Energy. This work was performed in part at MIT.nano.

AUTHOR DECLARATIONS

Conflict of Interest

The authors have no conflicts to disclose.

Author Contributions

Jack Van Sambeek: Conceptualization (equal); Data curation (lead); Formal analysis (lead); Investigation (lead); Methodology (equal); Visualization (lead); Writing – original draft (lead); Writing – review & editing (equal). **Jessica Dong:** Conceptualization (equal); Investigation (equal); Methodology (equal); Writing – review & editing (supporting). **Anton V. Ievlev:** Data curation (equal); Formal analysis (equal); Investigation (equal); Methodology (equal); Visualization (equal); Writing – review & editing (supporting). **Tao Cai:** Conceptualization (equal); Data curation (equal); Formal analysis (equal); Investigation (equal); Methodology (equal); Writing – review & editing (supporting). **Ida Sadeghi:** Investigation (supporting). **R. Jaramillo:** Conceptualization (equal); Funding acquisition (lead); Project administration (lead); Supervision (lead); Writing – review & editing (equal).

DATA AVAILABILITY

The data that support the findings of this study are openly available in Zenodo at https://doi.org/10.5281/zenodo.15585533, Ref. 28.

REFERENCES

[1]Y. Nishigaki, T. Nagai, M. Nishiwaki, T. Aizawa, M. Kozawa, K. Hanzawa, Y. Kato, H. Sai, H. Hiramatsu, H. Hosono, and H. Fujiwara, "Extraordinary strong band-edge absorption in distorted chalcogenide perovskites," Solar RRL **4**(5), 1900555 (2020).

[2]R. Bystrický, S. K. Tiwari, P. Hutár, and M. Sýkora, "Thermal stability of chalcogenide perovskites," Inorg. Chem. **63**(28), 12826–12838 (2024).

[3]S. Niu, J. Milam-Guerrero, Y. Zhou, K. Ye, B. Zhao, B. C. Melot, and J. Ravichandran, "Thermal stability study of transition metal perovskite sulfides," J. Mater. Res. **33**(24), 4135–4143 (2018).

[4]A. Jess, R. Yang, and C. J. Hages, "On the phase stability of chalcogenide perovskites," Chem. Mater. **34**, 6894 (2022).

[5]I. Sadeghi, J. Van Sambeek, T. Simonian, M. Xu, K. Ye, T. Cai, V. Nicolosi, J. M. LeBeau, and R. Jaramillo, "Expanding the perovskite periodic table to include chalcogenide alloys with tunable band gap spanning 1.5–1.9 eV," Adv. Funct. Mater. **33**(41), 2304575 (2023).

[6]R. Jaramillo and J. Ravichandran, "In praise and in search of highly-polarizable semiconductors: Technological promise and discovery strategies," APL Mater. **7**(10), 100902 (2019).

[7]K. Ye, I. Sadeghi, M. Xu, J. Van Sambeek, T. Cai, J. Dong, R. Kothari, J. M. LeBeau, and R. Jaramillo, "A processing route to chalcogenide perovskites alloys with tunable band gap via anion exchange," Adv. Funct. Mater. **34**(44), 2405135 (2024).

[8]A. Clearfield, "The synthesis and crystal structures of some alkaline earth titanium and zirconium sulfides," Acta Cryst. **16**(2), 135–142 (1963).

[9]R. Lelieveld and D. J. W. IJdo, "Sulphides with the $GdFeO_3$ structure," Acta Cryst. B **36** (10), 2223–2226 (1980).

[10]S. Niu, H. Huyan, Y. Liu, M. Yeung, K. Ye, L. Blankemeier, T. Orvis, D. Sarkar, D. J. Singh, R. Kapadia, and J. Ravichandran, "Bandgap control via structural and chemical tuning of transition metal perovskite chalcogenides," Adv. Mater. **29**(9), 1604733 (2017).

[11]S. Niu, B. Zhao, K. Ye, E. Bianco, J. Zhou, M. E. McConney, C. Settens, R. Haiges, R. Jaramillo, and J. Ravichandran, "Crystal growth and structural analysis of perovskite chalcogenide $BaZrS_3$ and Ruddlesden–Popper phase $Ba_3Zr_2S_7$," J. Mater. Res. **34**(22), 3819–3826 (2019).

[12]X. Wei, H. Hui, C. Zhao, C. Deng, M. Han, Z. Yu, A. Sheng, P. Roy, A. Chen, J. Lin, D. F. Watson, Y.-Y. Sun, T. Thomay, S. Yang, Q. Jia, S. Zhang, and H. Zeng, "Realization of $BaZrS_3$ chalcogenide perovskite thin films for optoelectronics," Nano Energy **68**, 104317 (2020).

[13]I. Sadeghi, K. Ye, M. Xu, Y. Li, J. M. LeBeau, and R. Jaramillo, "Making $BaZrS_3$ chalcogenide perovskite thin films by molecular beam epitaxy," Adv. Funct. Mater. **31**(45), 2105563 (2021).

[14]M. Surendran, H. Chen, B. Zhao, A. S. Thind, S. Singh, T. Orvis, H. Zhao, J.-K. Han, H. Htoon, M. Kawasaki, R. Mishra, and J. Ravichandran, "Epitaxial thin films of a chalcogenide perovskite," Chem. Mater. **33**(18), 7457–7464 (2021).

[15]K. Ye, B. Zhao, B. T. Diroll, J. Ravichandran, and R. Jaramillo, "Time-resolved photoluminescence studies of perovskite chalcogenides," Faraday Discuss. **239**, 146 (2022).

[16]K. Ye, N. Z. Koocher, S. Filippone, S. Niu, B. Zhao, M. Yeung, S. Bone, A. J. Robinson, P. Vora, A. Schleife, L. Ju, A. Boubnov, J. M. Rondinelli, J. Ravichandran, and R. Jaramillo, "Low-energy electronic structure of perovskite and Ruddlesden–Popper semiconductors in the Ba–Zr–S system probed by bond-selective polarized x-ray absorption spectroscopy, infrared reflectivity, and Raman scattering," Phys. Rev. B **105**(19), 195203 (2022).

[17]C. Comparotto, P. Ström, O. Donzel-Gargand, T. Kubart, and J. J. S. Scragg, "Synthesis of $BaZrS_3$ perovskite thin films at a moderate temperature on conductive substrates," ACS Appl. Energy Mater. **5**(5), 6335–6343 (2022).

[18]A. A. Pradhan, M. C. Uible, S. Agarwal, J. W. Turnley, S. Khandelwal, J. M. Peterson, D. D. Blach, R. N. Swope, L. Huang, S. C. Bart, and R. Agrawal, "Synthesis of $BaZrS_3$ and $BaHfS_3$ chalcogenide perovskite films using single-phase molecular precursors at moderate temperatures," Angew. Chem. Int. Ed. **62**(15), e202301049 (2023).

[19]B. Zhao, H. Chen, R. Ahsan, F. Hou, E. R. Hoglund, S. Singh, M. Shanmugasundaram, H. Zhao, A. V. Krayev, H. Htoon, P. E. Hopkins, J. Seidel, R. Kapadia, and J. Ravichandran, "Photoconductive effects in single crystals of $BaZrS_3$," ACS Photonics **11**(3), 1109–1116 (2024).

[20]K. Ye, M. Menahem, T. Salzillo, F. Knoop, B. Zhao, S. Niu, O. Hellman, J. Ravichandran, R. Jaramillo, and O. Yaffe, "Differing vibrational properties of halide and chalcogenide perovskite semiconductors and impact on optoelectronic performance," Phys. Rev. Mater. **8**(8), 085402 (2024).

[21]Z. Yuan, D. Dahliah, R. Claes, A. Pike, D. P. Fenning, G.-M. Rignanese, and G. Hautier, "Assessing carrier mobility, dopability, and defect tolerance in the chalcogenide perovskite $BaZr_3$," PRX Energy **3**(3), 033008 (2024).

[22]G. Aggarwal, A. S. Mirza, S. Riva, C. Comparotto, R. J. W. Frost, S. Mukherjee, M. Morales-Masis, H. Rensmo, and J. S. Scragg, "Charge transport and defects in sulfur-deficient chalcogenide perovskite $BaZrS_3$," arXiv:2405.17327 (2024).

[23]K. Hanzawa, S. Iimura, H. Hiramatsu, and H. Hosono, "Material design of green-light-emitting semiconductors: Perovskite-type sulfide $SrHfS_3$," J. Am. Chem. Soc. **141** (13), 5343–5349 (2019).

[24]I. M. Herz, "Charge-carrier mobilities in metal halide perovskites: Fundamental mechanisms and limits," ACS Energy Lett. **2**(7), 1539–1548 (2017).

[25]P. Y. Yu and M. Cardona, *Fundamentals of Semiconductors; Graduate Texts in Physics* (Springer, Berlin, 2010).

[26]M. Surendran, S. Singh, H. Chen, C. Wu, A. Avishai, Y.-T. Shao, and J. Ravichandran, "A hybrid pulsed laser deposition approach to grow thin films of chalcogenides," Adv. Mater. **36**(19), 2312620 (2024).

[27]S. Filippone, B. Zhao, S. Niu, N. Z. Koocher, D. Silevitch, I. Fina, J. M. Rondinelli, J. Ravichandran, and R. Jaramillo, "Discovery of highly polarizable semiconductors $BaZrS_3$ and $Ba_3Zr_2S_7$," Phys. Rev. Mater. **4**(9), 091601 (2020).

[28]J. Van Sambeek, J. Dong, A. Ievlev, T. Cai, I. Sadeghi, and R. Jaramillo (2025). "Data for 'electronic mobility, doping, and defects in epitaxial $BaZrS_3$ chalcogenide perovskite thin films'," Zenodo, Dataset https://doi.org/10.5281/zenodo.15585533